

Anomaly Detection with Deep Perceptual Autoencoders

Nina Tuluptceva, Bart Bakker, Irina Fedulova, Heinrich Schulz, and Dmitry V. Dylov, *Member, IEEE*

Abstract—Anomaly detection is the problem of recognizing abnormal inputs based on the seen examples of normal data. Despite recent advances of deep learning in recognizing image anomalies, these methods still prove incapable of handling complex images, such as those encountered in the medical domain. Barely visible abnormalities in chest X-rays or metastases in lymph nodes on the scans of the pathology slides resemble normal images and are very difficult to detect. To address this problem, we introduce a new powerful method of image anomaly detection. It relies on the classical autoencoder approach with a re-designed training pipeline to handle high-resolution, complex images, and a robust way of computing an image abnormality score. We revisit the very problem statement of fully unsupervised anomaly detection, where no abnormal examples are provided during the model setup. We propose to relax this unrealistic assumption by using a very small number of anomalies of confined variability merely to initiate the search of hyperparameters of the model. We evaluate our solution on natural image datasets with a known benchmark, as well as on two medical datasets containing radiology and digital pathology images. The proposed approach suggests a new strong baseline for image anomaly detection and outperforms state-of-the-art approaches in complex pattern analysis tasks.

Index Terms—Anomaly Detection, Autoencoders, Chest X-Rays, Radiology, Digital Pathology

1 INTRODUCTION

ANOMALY detection is a crucial task in the deployment of machine learning models, where knowing the “normal” data samples should help spot the “abnormal” ones [8], [10]. If an input deviates from the training data substantially, it is usually impossible to predict how the model will behave [5], [32]. This makes it essential for high-consequence applications, such as medical decision support systems, to know how to recognize the anomalous data. Identification of rare occurrences is another important application where anomaly detection is useful. For example, in pathology, where labeling diverse microscopy datasets is both time-consuming and expensive, the rare types of cells and tissues require specialized expertise from the annotator [14], [25]. Because the normal cases greatly prevail over the abnormal one, anomaly detection algorithms can largely alleviate the annotation burden and automatically point to the rare samples.

In recent years, deep learning techniques achieved important advances in image anomaly detection [16], [17], [33], [35], [36], [38], [41], [46]. However, these efforts were primarily focused on artificial problems with distinct anomalies in natural images (e.g., outliers in images of “cats” in the CIFAR10 dataset [26], see Figure 1). The medical anomalies, however, differ from those in the natural images [33], [38], [39]. The medical image anomalies tend to resemble the normal data much more strongly, being much “closer” to them by the distribution. For example, detection of obscure neoplasms in chest X-rays [43] and of metastases in H&E-stained lymph node images [7] manifest a blatant challenge at hand, with the anomalous tissues being barely different from the normal ones (see Figure 1). Only recently a few

groups started dedicating their effort to the problem [33], [38]. However, to the best of our knowledge, a thorough comparison of state-of-the-art (SOTA) solutions in the medical domain is still missing.

In our paper, we evaluate and compare strongest SOTA approaches ([38], [41] and [33]) on the two aforementioned medical tasks. We find these methods either to struggle detecting such types of abnormalities, or to require a lot of time and resources for training. Besides, the SOTA approaches lack a robust way of setting up model hyperparameters on new datasets, which complicates their use. Thus, we revisit the problem of image anomaly detection and introduce a new powerful approach, capable of tackling these challenges in the medical domain. The proposed method leverages the efficacy of *autoencoders* for anomaly detection [20], the expressiveness of *perceptual loss* [22] for understanding the content in the images, and the power of the *progressive growth* [23] to handle training on high-dimensional image data.

Recent related studies showed the effectiveness of deep features as a perceptual metric between images (perceptual loss), and as a score of anomaly [15], [22], [41], [47]. Also, the use of the perceptual loss for training autoencoders has been very popular in a variety of tasks [9], [21], [22], [41], [47] except for the task of anomaly detection which has been inexplicably somewhat dismissed so far. Trained only on normal data, autoencoders tend to produce a high reconstruction error between the input and the output when the input is an abnormal sample. That property has been used intensively for anomaly detection [13], [17], [35], [46], [48]. We propose to compel the autoencoder to reconstruct *perceptive* or *content* information of the normal images, by using *only* the perceptual loss during autoencoder training. As such, the reconstructed image may not be an image altogether, but a tensor that stores the “content” of the input

N. Tuluptceva is with Philips Research and with Skolkovo Institute of Science and Technology, Moscow, Russia, 121205. B. Bakker, I. Fedulova, and H. Schulz are with Philips Research. D. V. Dylov is with Skolkovo Institute of Science and Technology, e-mail: d.dylov@skoltech.ru.

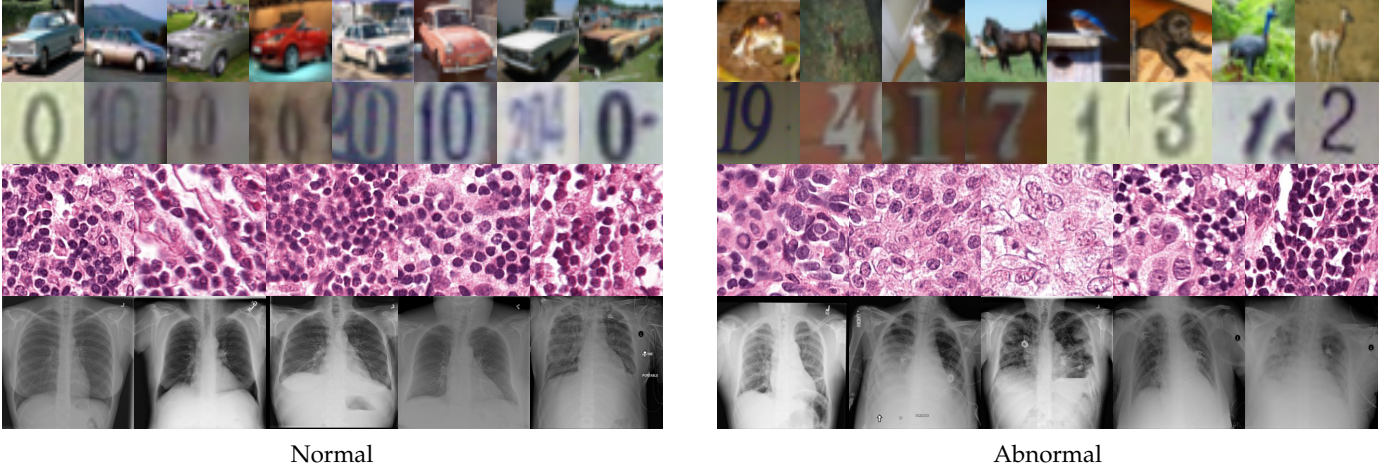


Fig. 1: Examples of normal vs. abnormal images of considered datasets. Natural images: (first row) cars vs other classes of CIFAR10 dataset [26], (second row) digits “0” vs digits “1” – “9” of SVHN dataset [31]. Medical images: (third row) healthy tissue vs. tissue with metastases in H&E-stained lymph node of Camelyon16 challenge [7], (fourth row) normal chest X-rays vs. chest X-rays with abnormal findings of NIH dataset [43].

image. The main idea behind it is not to force the network to reconstruct a realistic looking image, but to let it be flexible in understanding the content of the normal data. Section 3.1 covers the details.

To further improve the expressiveness of the autoencoder and to allow it to capture even the fine details in the data, we propose to train the model using progressive growing technique [19], [23], starting from a low-resolution network and adding new layers to gradually introduce additional details during the training. In particular, we present how to achieve a smooth growth of perceptual information in the loss function, and show that this greatly improves the quality of anomaly detection in the high-resolution medical data. We will describe it in Section 3.2.

Lastly, we propose a new approach to the basic setup of anomaly detection model. Most approaches [16], [35], [36], [41], [46] prescribe not to use any anomaly examples during the model setup, dismissing the questions of optimization and of hyperparameter selection for such models. However, in reality, some types of abnormalities to detect are actually known (for example, the most frequent pathologies on the chest X-rays). Therefore, we consider the *weakly-supervised* scenario where a low number of anomalies with confined variability are available for use in optimal model hyperparameter selection (Section 3.3). We believe this scenario reflects the real tasks encountered in practice, provides a clear pipeline for setting up the model on new data, and helps to obtain reproducible results.

To summarize our main results quantitatively, the proposed solution achieves 0.943 ROC AUC in the detection of metastases in H&E stained images of lymph nodes (Camelyon16 dataset [7]), and 0.926 in the detection of abnormal chest X-rays (subset of NIH dataset [43]). This outperforms SOTA methods.

2 RELATED WORK

Anomaly detection has been extensively studied in a wide range of domains, including but not being limited to fraud

detection [2], cyber-intrusion detection [27], anomaly detection in videos [24], financial domain [3], and for the Internet of Things [30]. An extensive survey is out of our paper’s scope and can be found in [8], [10]. Here we will focus on anomaly detection in images.

Distribution-based methods. Conceptually, abnormal examples lie in low probability density areas of the “normal” data distribution; samples with a lower probability are thus more likely to be an anomaly. Distribution-based methods try to predict if the new example lies in the high-probability area or not. KDE [34] or a Gaussian mixture models (GMM) [29] aims to model data distribution directly. One-class SVM [12], Isolation Forest [28], SVDD [40] methods create a boundary around normal examples. The latest methods extend classical solutions by using deep data representation. For example, Deep IF [33] successfully utilized Isolation Forest on features extracted from a deep pre-trained network. DAGMM [49] proposed to use GMM on learned data representation. Deep SVDD [36] trains a network representation to minimize the volume of a hypersphere of the normal samples. However, the most critical part of such approaches is given in learning discriminative data representation. As shown in [33] anomaly detection performance may drop if there is a domain shift between the source dataset (for training data representation) and the target task.

Reconstruction-based methods. PCA and autoencoder-based [44] methods rely on the fact that the model trained only on normal data can not accurately reconstruct anomalies. GAN’s-based methods (such as AnoGAN [38]) utilizes a similar idea: the generator, trained only on normal data, could not generate abnormal images. The reconstruction error indicates abnormalities. The latest methods broadly extend this idea by utilizing different combinations of autoencoders and adversarial losses of GAN’s (OCGAN [35], GANomaly [4], ALOCC [37], DAOL [39] PIAD [41]), variational or robust autoencoders [48], energy-based models (DSEBM [46]), probabilistic interpretation of the latent space [1], [6], bi-directional GANs [45], memory blocks [17],

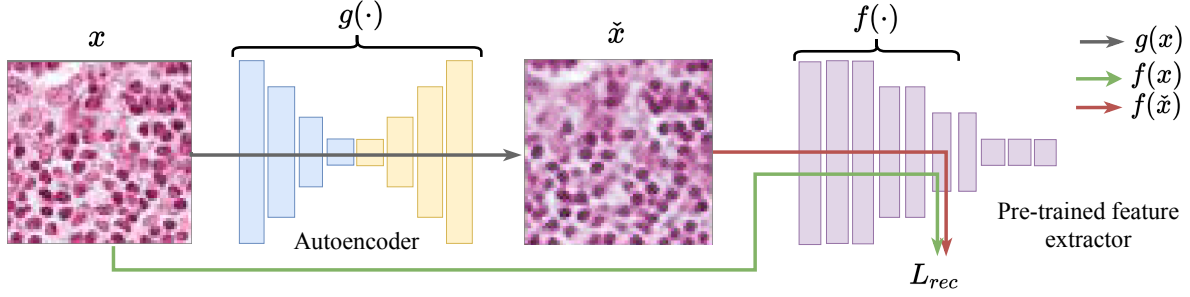


Fig. 2: The proposed Deep Perceptual Autoencoder for image anomaly detection: g denotes the autoencoder network, f denotes a feature extractor, x is an image, and $\hat{x} = g(x)$ is a reconstructed “image”. Reconstruction loss L_{rec} calculates difference between deep features $f(x)$ and $f(\hat{x})$.

etc. The main difficulties of such approaches are given in choosing an effective dissimilarity metric and searching for the right degree of compression (size of bottleneck). The [47] shows the extraordinary effectiveness of deep features as a perceptual dissimilarity metric. However, in anomaly detection, the use of perceptual loss is unreasonably missed. For the best of our knowledge, only [41] utilizes a perceptual metric for the anomaly detection task. We believe that powerful dissimilarity measure is key-component of reconstruction based methods. Our work shows that a combination of a deep autoencoder and the perceptual loss (without any other tricks) yields a simple and effective anomaly detection performance baseline.

A recent model Deep GEO [16] employed a new method of image anomaly detection based on the idea of the self-supervised learning. The authors proposed to create a self-labeled dataset by applying different geometric transformations to images: each geometric transformation (rotating on 90 degrees, rotating on 180 degrees, etc.) – a new class of dataset. After training a classifier on such a self-labeled dataset, the abnormality of a new input is predicted as the average quality of classification its geometric transformations.

Despite a large number of anomaly detection methods that appeared in the recent years, only several papers [11], [11], [33], [39] considered medical images. Nevertheless, usually, they miss the comparison with the latest strongest approaches on the considered medical task. Another problem is that there is no standardized benchmark for the medical anomaly detection challenge. Herein, we fill this gap by implementing SOTA methods and by comparing their performance on two medical problems with different types of abnormalities.

3 METHOD

3.1 Deep Perceptual Autoencoder

Autoencoder-based approaches rely on the fact that autoencoders can learn shared patterns of the normal images and, then, restore them correctly. The key idea of our method is to simplify the learning of these common factors inherent to the data, by providing a loss function that measures “pattern”-dissimilarity of the input and the output. It was shown that the perceptual loss – which computes a distance between the deep features obtained from an object classification neural network pre-trained on a large diverse dataset

– can capture the “content” dissimilarity of the images [15], [22]. We further propose to use *only* the perceptual loss to train the autoencoder and to compute the restoration error during the evaluation, without considering the loss term that compels to restore the whole input information in an image. We will show that such a loss allows the autoencoder more flexibility to gain a meaningful understanding of the “normality” of the data, leading to much better results.

Figure 2 illustrates our approach, which we called Deep Perceptual Autoencoder. Let g be the autoencoder network, and x be an image. During the training, the autoencoder minimizes the difference between x and the reconstructed “image” $\hat{x} = g(x)$, being called the reconstruction loss $L_{rec}(x, \hat{x})$. To compute the perceptual loss as the reconstruction loss between x and \hat{x} , we compute the difference between the deep features of these images ($f(x)$ and $f(\hat{x})$, respectively). We adopt relative-perceptual-L1 loss from Ref. [41] as it is robust to noise and to the changes in the image contrast perceptual metric: $L_{rec}(x, \hat{x}) = \frac{\|\hat{f}(x) - \hat{f}(\hat{x})\|_1}{\|\hat{f}(x)\|_1}$, where $\hat{f}(x) = \frac{f(x) - \mu}{\sigma}$ are the normalized features with pre-calculated on a large dataset the mean μ and the standard deviation σ of the filter responses of the layer. In the evaluation stage, the same $L_{rec}(x, g(x))$ is used to predict the abnormality in the new input x .

3.2 Progressive Growing

To improve the expressive power of the autoencoder in Figure 2, we propose to train it by harnessing the power of progressive growth [23]. Illustrated in Figure 3, the suggested pipeline gradually *grows* the “level” of the “perceptual” information in the loss function. In the beginning of the training, the loss function computes the dissimilarity between the low-resolution images using the features from the coarse layers of the network, whereas, as the training advances, the “level” of this information is increased by including deeper and deeper features. It seems intuitively essential because the “content” information is absent in the low-resolution images, with only the main color and the high-level structure being stored there. The novelty that we propose in our solution, therefore, is to *synchronize* addition of the new layers to the autoencoder with the gradual increase of the depth of the features entailed in the calculation of the perceptual loss (see Figure 3(Right) below).

Both the autoencoder g and the perceptual loss L_{rec} have a low “resolution” in the beginning (Figure 3(Left)). For

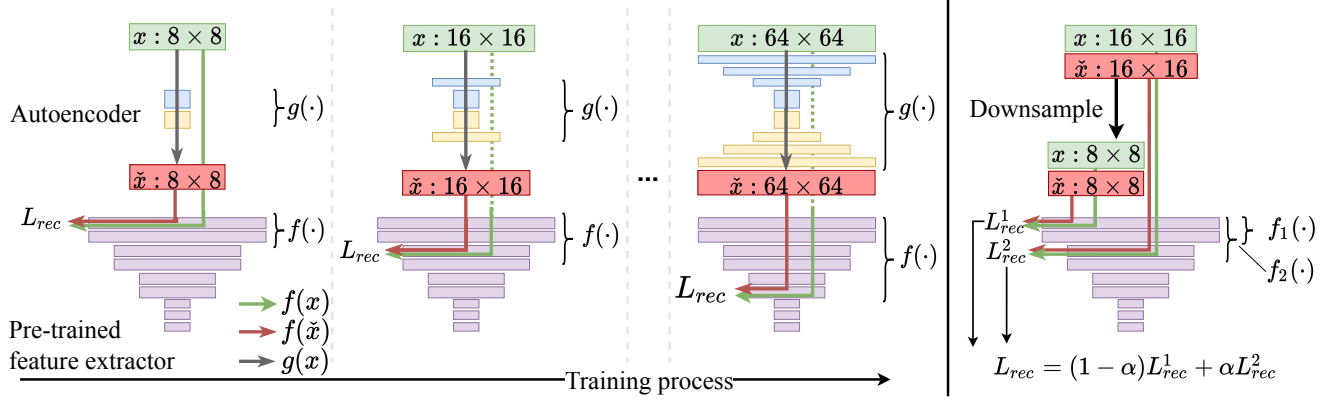


Fig. 3: Progressive training process. (Left) The layers are incrementally faded to the autoencoder g , and the depth of the features f increases synchronously. (Right) The gradual increase of the “resolution” of the perceptual loss L_{rec} .

example, the input and the output of the autoencoder are 8×8 -pixel images x and \tilde{x} , and the loss L_{rec} computes the distance between the features $f(x)$ and $f(\tilde{x})$ of the coarse layer f (the pre-trained feature extractor network). As the training advances, the layers are incrementally added to the autoencoder g , and the depth of the features f is increased.

While doubling the resolution of the autoencoder, for example, from 8×8 to 16×16 , the new layers are introduced smoothly, with the parameter α linearly increasing from 0 to 1 [19], [23]. As it was proposed in [19], [23], during this process, both the input x and the output \tilde{x} are the mixtures of the new high-resolution 16×16 image and the previous low-resolution 8×8 image, upsampled by a factor of two (not shown in Figure). In a similar manner, we smoothly increase the “level” of information supplied to L_{rec} from the features f_1 to the features f_2 : $L_{rec} = \alpha * L_{rec}(f_2(x), f_2(\tilde{x})) + (1 - \alpha) * L_{rec}(f_1(\text{down}(x)), f_1(\text{down}(\tilde{x})))$, where $\text{down}(\cdot)$ carries out the downsampling by a factor of two.

3.3 Hyperparameters Tuning

Any anomaly detection model has many hyperparameters, the tuning of which is essential for the quality of the detection (in our method, these are the number of convolutions in the autoencoder, the size of the bottleneck, etc.). The majority of the anomaly detection papers declare no need to see the abnormal examples to set up their models, remaining vague with regard to how to choose the hyperparameters and how to deal with those cases when some new data needs to be analyzed by the same model. Some works mention tuning hyperparameters based on an unsupervised metric, like the value of the restoration error in the reconstruction-based methods [33], [35]. However, lower reconstruction loss does not mean better anomaly detection quality. For example, better reconstruction due to a larger bottleneck can cause the autoencoder to reconstruct anomalous data accurately as well.

In practice, however, one can have access to some labeled anomalies during the model setup. The number of such examples may be small, and they may not represent all possible abnormalities in the data, so it is typically tricky to use them in training. In our work, we formulate a new *weakly-supervised* training scenario where a low number of labeled anomalous examples of a limited variation (i.e., a confined

number of the types of anomalies) is available during the model setup as a “validation” or an “optimization” set. This small set serves a single purpose – select the model’s hyperparameters during its setup. Unlike works [33], [39] that use a small subset of *all* anomalous data to improve the performance, we propose to use a small subset of *limited* types of anomalies merely for the initiation. This is a key difference because, in practice, it is difficult to cover all types of anomalies, even with just several examples of each. We believe that the proposed setting reflects real-world scenarios, allows consistent structuring of the experiments, and enables the generation of reproducible results.

4 EXPERIMENTS

4.1 Datasets and Evaluation Protocol

We evaluated approaches in the problem statement of novelty detection, where the training data are assumed to be free of anomalies.

4.1.1 Medical Images

To perform an extensive evaluation of anomaly detection methods in the medical domain, we examined two challenging medical problems with different image characteristics and abnormality appearance.

4.1.1.1 Metastases Detection in Digital Pathology: Detecting metastases of lymph nodes is an extremely important variable in the diagnosis of breast cancer. However, the examination process is time-consuming and challenging. Figure 1 shows examples of the tumor and normal tissues. Tissue with metastasis may differ from healthy one only by texture, spatial structure, or distribution of nuclei, and can be easily confused with normal tissue. We considered the task of detecting metastases in H&E stained images of lymph nodes in the Camelyon16 challenge [7]. We trained anomaly detection models only on healthy tissue aiming to identify tissue with metastases. The training dataset of Camelyon16 consists of 110 whole-slide images (WSIs) contained tumors, and 160 are not, and testing dataset with 80 regular slides and 50 slides containing metastases. For all slides, we performed the following preprocessing. Firstly, we divided tissue from the background by applying Otsu’s thresholding. Then we sampled 768×768 tiles (maximum

50 from one slide) of healthy tissue (from entirely normal images) and tumor tissue (from slides with metastases) and performed color normalization [42]. For the hyperparameter search we sampled tiles only from 4 out of 110 train tumor slides (validation set of confined variability). We obtained 7612 normal training images, 200 tumor images for validation, and 4000 (normal) + 817 (tumor) images for the test. During training, we randomly sampled 256x256 crops from 768x768 normalized tiles, and to the test, we used only a central 256x256 crop (to reduce border effect during normalization). The original WSIs were done with 40x magnification of tissue, but during the hyperparameter search, we also considered x10 and x20 magnification by bilinear downsampling images (256x256 to 128x128, and 64x64).

4.1.1.2 Anomaly Detection on Chest X-Rays: Chest X-ray is one of the most common examinations for diagnosing various lung diseases. We considered the task of the recognition of fourteen findings, such as Atelectasis or Cardiomegaly, on the chest X-rays in the NIH dataset [43] (Figure 1). Searching abnormalities on a chest x-ray is challenging even for an experienced radiologist since abnormality may occupy only a small region of lungs, or be almost invisible. The dataset consists of 112,120 frontal-view images of 30,805 unique patients: 86523 for training, 25595 for evaluation. We split the dataset into two sub-datasets having only posteroanterior (PA) or anteroposterior (AP) projections, because organs on them look differently. We tried different preprocessing during the hyperparameter search: rescaling to 256x256, 128x128, and 64x64 and histogram equalization, central crop (3/4 of the image size) to delete “noisy” borders. We considered images without any disease marker as “normal” and used them for training. As abnormal image for hyperparameter search, we used the training images of most frequent disease (‘Infiltration’) out of fourteen possibilities. We also evaluated model on subset containing “clearer” normal/abnormal cases, provided by [39]. This subset consist on 4261 normal images for training, 849 normal and 857 abnormal images for validation, and 677 normal and 677 abnormal images for testing.

4.1.2 Natural Images

We also evaluate the methods on two natural image benchmarks CIFAR10 [26] and SVHN [31]. Both datasets provide an official train-test split and consist of 10 classes. Following previous works, we used a one-vs-all evaluation protocol: we design 10 different experiments, where only one class is alternately considered as normal, while others treated as abnormal. In all experiments, we rescaled images to 32x32 resolution. During the hyperparameter search, we considered conversion images to grayscale. We randomly sampled one abnormal class of the train set as a validation set with abnormal images (that has only one type of abnormalities out of nine). These conditions were fixed in all methods compared beneath.

4.2 Baselines.

We considered the following strongest SOTA baselines of different paradigms: Deep GEO [16] Deep IF [33] and PIAD [41]. On natural images we also competed against

AnoGAN [38], GANomaly [4], DAGMM [49], DSEBM [46], and DeepSVDD [36] methods. On the NIH dataset, also compared our results to DAOL framework [18], [39], purposely developed for detecting anomalies in chest X-rays.

4.3 Implementation details.

We implemented Deep IF and PIAD approaches using extensive descriptions provided by authors. For GANomaly and Deep GEO, we adapted the official code for our experiment setups. Results of DAOL method were obtained in the corresponding paper. For other approaches, we used results as reported in [33]. For the strongest baselines, we also perform a hyperparameter search as it was proposed in our paper. For the Deep GEO approach, we searched for an optimal number of the classifier’s training epochs (we find the method to be sensitive to this parameter). For Deep IF, we searched for the best feature representation – the best layer of the feature extractor network. For PIAD, we searched for the optimal size of the latent vector, the best feature layer in the relative-perceptual-L1 loss, and the best number of training epochs. Also, for all algorithms, we searched for the best image preprocessing.

For the proposed approach, in all experiments, we used autoencoders with pre-activation residual blocks. For the computation of the relative-perceptual-L1 loss, we used the VGG19 network that was pre-trained on ImageNet. We trained the autoencoder until after the loss on the hold-out set of normal images stops decreasing. During the hyperparameter selection, we search for the best size of the autoencoder bottleneck and for the best feature layer of relative-perceptual-L1 loss. Further details will be covered in the released algorithm code.

Hyperparameter search was performed by 3-fold cross-validation by maximizing ROC AUC. Only in experiments on NIH subset, provided by [39], we didn’t perform cross-validation but run experiment 3 times on the same train-validation split to repeat DAOL experiment settings.

4.4 Results

4.4.1 Natural Images

As mentioned above, for CIFAR10 and SVHN datasets, we conducted ten experiments, where each class alternatively was considered normal. In such experiments, an anomaly is an image of an object of a different class. Therefore, abnormal images are very different from normal data (compared to anomalies on medical images), but normal data also have high variability. The average results over all experiments in a dataset are reported in Table 1. The detailed table with ROC AUC per each experiment is in the Appendix, Table 5. Notice, while testing on these datasets, we do not use progressive growth in our method.

The approaches that we called the strongest baselines (Deep GEO, PIAD, Deep IF) and our method significantly outperform other methods, with margin 20% (except for Deep IF on SVHN dataset). The Deep GEO approach, which classifies the geometric transformations of images, excels in distinguishing digits from each other (SVHN dataset). The reason for that is that digits have a simple geometrical structure, and their geometric transformations are easily

	AnoGAN	GANomaly	DAGMM	DSEBM	DeepSVDD	DeepGEO	PIAD	Deep IF	Ours (w/o p. g.)
CIFAR10	57.6/-	58.1/-	57.5/-	64.8/-	58.8/-	86.6/86.5	78.8/81.3	87.2/87.3	83.9
SVHN	53.3/-	-	51.8/-	57.3/-	57.1/-	93.3/93.5	77.0/76.3	59.0/62.4	80.3

TABLE 1: ROC AUC in % for CIFAR10 and SVHN datasets averaged over all ten experiments in the dataset (see Section 4.1.2) and over three different runs per experiment (each experiment we repeated three times with different model initialization). For methods results are reported in two options: ROC AUC obtained with authors’ default hyperparameters (left), ROC AUC obtained with hyperparameters found by cross-validation (right).

	Deep GEO	PIAD	Deep IF	Ours (w/o p. g.)	Ours (with p. g.)
Camelyon16	52.4 ± 11.1/45.9 ± 2.1	85.4 ± 2.0/89.5 ± 0.6	87.6 ± 1.5/90.6 ± 0.3	92.7 ± 0.4	93.4 ± 0.3
NIH (a subset)	85.8 ± 0.6/ 85.3 ± 1.0	88.0 ± 1.1/87.3 ± 0.9	76.6 ± 2.7 /85.3 ± 0.4	92.0 ± 0.2	92.6 ± 0.2
NIH (PA proj.)	60.2 ± 2.6/63.6 ± 0.6	68.0 ± 0.2/68.7 ± 0.5	52.2 ± 0.5/47.2 ± 0.4	70.3 ± 0.2	70.8 ± 0.1
NIH (AP proj.)	53.1 ± 0.3/54.4 ± 0.6	57.4 ± 0.4/58.6 ± 0.3	54.3 ± 0.5/56.1 ± 0.2	58.6 ± 0.1	58.5 ± 0.0

TABLE 2: ROC AUC in % with standard deviation (over 3 runs). For baselines results are reported in two options: ROC AUC obtained with authors’ default hyperparameters (left), ROC AUC obtained with hyperparameters found by cross-validation (right). For our method, results are showed with and without progressive growing regime of training.

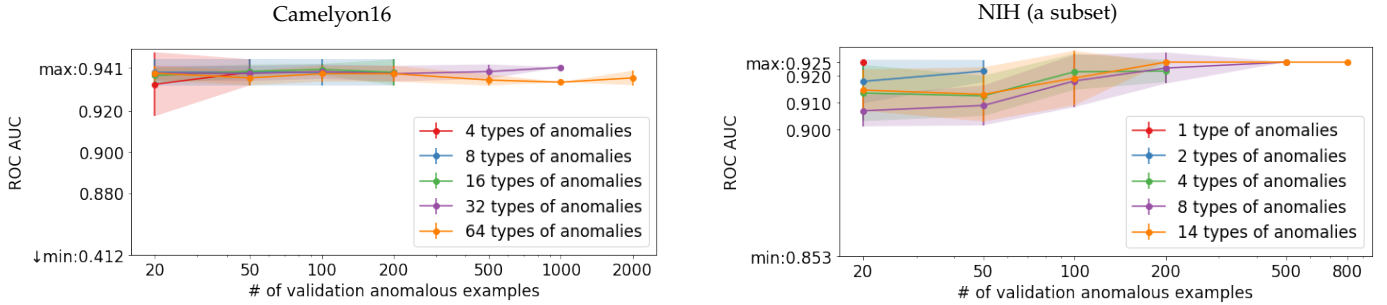


Fig. 4: Dependence of the quality of anomaly detection (of our approach) on the number of anomaly examples s (the x-axis) and their variability (the different lines) in the validation set. The highest (max) and the lowest (min) performance achievable on these hyperparameter spaces are shown on the plots. For Camelyon16, we considers metastases tiles from one slide as abnormality of one type, for NIH dataset, type of abnormality is unique finding. We used the same 3-fold cross-validation split and hyperparameter space as in previous experiments. We sampled a validation set for each configuration (# anomaly types, # anomaly examples) seven times. For each sample of the validation set, we selected the best hyperparameters on the cross-validation split. Then we evaluated the quality of the model trained on all training images with chosen hyperparameters on test split. Here we showed mean and std of test ROC AUC’s (computed over three samples of the validation set for this configuration)

	PIAD	Ours (w/o p. g.)	Ours (with p. g.)
Camelyon16	84	105	160
NIH (a sub.)	287	59	177
NIH (PA proj.)	151	89	159
NIH (AP proj.)	275	70	107

TABLE 3: Average training time (minutes). Experiments were run on GeForce GTX 1080 Ti with Pytorch 1.4.0.

distinguishable. Our approach shows the second-best result. However, Deep IF fails – features obtained by pre-trained on ImageNet neural network turned out to be not discriminative for this task.

Images of CIFAR10 dataset have a more challenging geometrical structure than SVHN ones, so Deep GEO shows lower performance. However, since the domain shift between ImageNet and CIFAR10 dataset is smaller, Deep IF also shows good results. Our method closely follows for the leaders Deep GEO and Deep IF. We noticed that our approach in both datasets outperformed PIAD by 3%.

We noted that reconstruction-based approaches, like ours and PIAD, are inferior to Deep GEO for such tasks.

We hypothesize that due to the high variability of normal images, the autoencoder overgeneralizes on anomaly data. Indeed, during hyperparameter tuning, we search for optimal autoencoder capacity, where the autoencoder reconstructs normal data well but does not generalize on other data. However, when training data are highly variable, the autoencoder generalizes better and on unseen classes.

Interestingly that the hyperparameter cross-validation does not almost improve the quality of baselines methods. It seems like the author’s default hyperparameters are almost the best for these datasets.

4.4.2 Medical Images

As Deep GEO, PIAD, and Deep IF are superior to other methods with a large margin on natural image datasets, we chose them for evaluation medical images. We presented results in Table 2. For our method, we provided results obtained with and without progressive growing training regime.

Remarkably, our approach significantly outperforms Deep GEO and Deep IF in both medical datasets. The Deep GEO shows poor performance on the digital pathology data, where the images are invariant to geometric transforma-

	Camelyon16	NIH (a subset)	NIH (PA proj.)	NIH (AP proj.)
(1) L1 + unsupervised	21.1 \pm 1.4	70.8 \pm 0.6	66.5 \pm 0.1	52.4 \pm 0.1
(2) PL + unsupervised	87.9 \pm 0.6	89.3 \pm 0.2	68.9 \pm 0.1	56.4 \pm 0.2
(3) PL + weakly-supervised	92.7 \pm 0.4	92.0 \pm 0.2	70.3 \pm 0.2	58.6 \pm 0.1
(4) PL + 1 \cdot adv + weakly-supervised	79.4 \pm 4.0	64.4 \pm 7.8	52.3 \pm 3.3	51.5 \pm 3.4
(5) PL + 0.1 \cdot adv + weakly-supervised	90.8 \pm 0.7	82.2 \pm 2.6	59.2 \pm 1.4	55.4 \pm 0.9
(6) PL + 1 \cdot L1 + weakly-supervised	75.3 \pm 1.6	91.7 \pm 0.4	70.7 \pm 0.2	57.3 \pm 0.1
(7) PL + 0.1 \cdot L1 + weakly-supervised	93.0 \pm 0.3	92.0 \pm 0.1	70.6 \pm 0.2	58.5 \pm 0.1
(8) PL + 1 \cdot L1 + 1 \cdot adv + weakly-supervised	57.5 \pm 6.3	59.3 \pm 5.0	50.1 \pm 2.0	51.7 \pm 0.8
(9) PL + 0.1 \cdot L1 + 0.1 \cdot adv + weakly-supervised	90.6 \pm 1.0	78.2 \pm 1.0	60.8 \pm 1.8	55.5 \pm 0.4
(10) PL + weakly-supervised + progressive growing	93.4 \pm 0.3	92.6 \pm 0.2	70.8 \pm 0.1	58.5 \pm 0.0

TABLE 4: Ablation study. ROC AUC in % with standard deviation (over 3 runs).

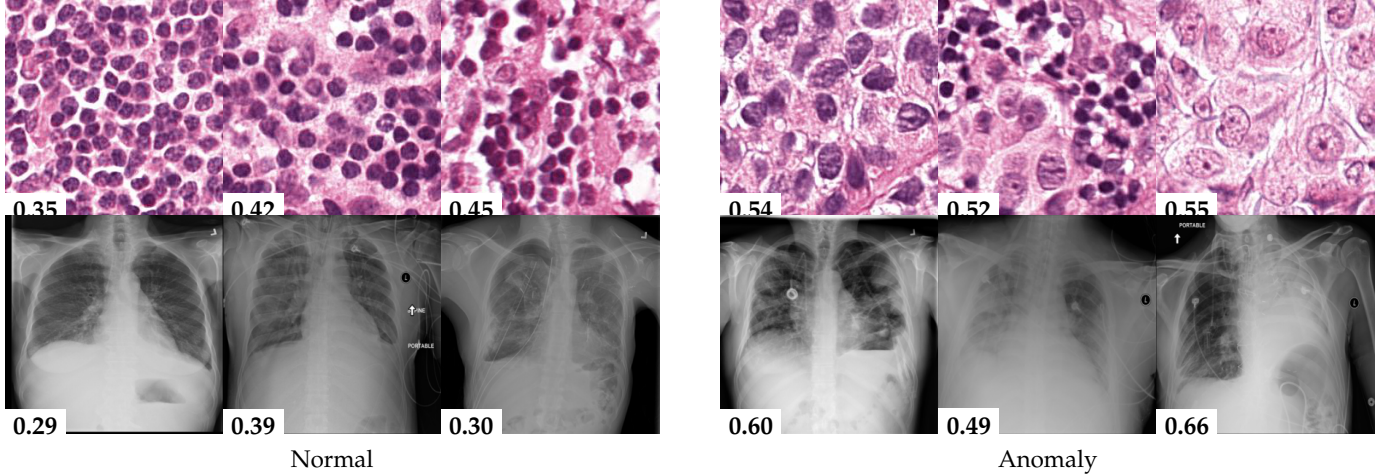


Fig. 5: Examples of normal (left) and anomaly (right) images of H&E-stained lymph node of Camelyon16 challenge [7] (top) and chest X-rays of NIH dataset [43] (bottom). We also showed the predicted anomaly score by the proposed method. The higher the score, the more likely to be an anomaly.

tions. Indeed, digital pathology scans do not have space orientation; rotations and translations of them are not distinguishable. We can tell that the Deep GEO is not applicable to such data. For NIH PA and AP projections, ROC AUC’s are also very low. Our hypothesis is that if abnormality occupy a small region of the image, the classifier still distinguishes the geometric transformations well, so the quality classification hardly indicates such abnormalities. For NIH (a subset) with more “obvious” abnormalities (the abnormal region is larger), the Deep GEO approach shows better results.

Deep IF failed on NIH (PA proj.) and NIH (AP proj.). Again probably due to domain shift between ImageNet and X-ray images, features obtained from the pre-trained network turned out to be not discriminative for this task. However, for the Camelyon16 and NIH (a subset) experiments, ROC AUC is quite high. We suggest that if the feature extractor network was pre-trained on more relative to X-ray image analysis task, Deep IF would show high performance on NIH (PA proj.) and NIH (AP proj.) experiments. We conclude that the weakest side of this approach is feature representation. Now, there is no explicit algorithm on how to obtain discriminative feature space for a different experimental setup.

With a smaller margin, our algorithm (in both options: with and without progressive growing) is also ahead of the PIAD method. However, we would like to highlight that our method, in general, easier and faster in training,

less resource-hungry, and higher performance. In contrast to these 4-network PIAD architectures, though, our method uses only encoder and decoder, allowing a much simpler model setup (no need to search for a schedule of the adversarial training) and demanding less computational resources (training takes two networks instead of four and goes faster without the need for discriminators). The average time of training of final models is provided in Table 3. Also, using progressive growing training, allowed us additionally to gain up 1% quality.

We illustrate the predictions of our model in Figure 5.

4.5 Hyperparameters Tuning Analysis

Proposing to use a small and restricted set of anomalies aka validation set during model setup, we were interested how many anomaly types and how many anomaly examples are required. In Figure 4 we showed dependence of the quality of anomaly detection on the number of anomaly examples and their variability in the validation set. The experiment shows that even small number abnormal samples (for example, 20) of one type of anomaly are enough, to reject “bad” hyperparameter configuration. In two considered experiments, having 20 examples of one type abnormalities very enough to choose hyperparameters with 2% quality of the best one.

4.6 Ablation study

To stress the importance of every component proposed herein, we performed an extensive ablation study. Table 4 considers ten ablation scenarios.

(1): Autoencoder (AE) training with the L1 loss and the hyperparameter optimization using *unsupervised* criteria (the reconstruction loss).

(2): The same, but where we changed L1 on perceptual loss (PL).

(3): The previous one with the hyperparameters corresponding to the best validation ROC AUC (*weakly-supervised* scenario).

(4)–(9): Here, we added the adversarial loss (with weights 1 and 0.1) or L1 norm, or both of them to the loss function during the training (to force the reconstructed image to have a realistic look or to restore the whole input image).

(10): The last training scenario finally considers the progressive growing.

Remarkably, the usage of the perceptual loss (2) win to the L1 norm (1) with a large margin. We also observe that the method of selecting the hyperparameters by revealing a subset of anomalies of confined variability (3), benefits the anomaly detection performance (compared to the unsupervised criteria (2)). We note the advantage of our approach compared to the autoencoder, which encourages fully restored or realistic looking images (4)–(9) (using additional adversarial or L1 norm loss). By our hypothesis, the usage only the perceptual loss to train the autoencoder without considering additional the L1 or the adversarial term that compels to restore the realistic looking images allows an autoencoder more flexibility to gain a meaningful understanding of the “normality”. And in these experiments we demonstrated that such additional losses only decrease performance. Finally, the proposed progressive growing technique (10) allow us to gain additional performance.

5 CONCLUSIONS

In this paper, we evaluated a range of state-of-the-art image anomaly detection methods, the performance of which we found to be sub-optimal in the challenging medical problems. We proposed a new method that uses an autoencoder to understand normal data representation, with optimization being performed with regard to perceptual loss in the regime of progressive growing training. To overcome the problem of setting up the model on new data, we propose to use a small set of anomalous examples of a limited variation – just to select the model’s hyperparameters. We believe that this realization reflects real-world scenarios, allowing consistent structuring of the experiments, and enabling the generation of reproducible results in the future. The proposed approach achieved 0.943 ROC AUC in the detection of metastases and 0.926 in the detection of abnormal chest X-rays. Our work establishes a new strong baseline for image anomaly detection.

APPENDIX A

The detailed results with ROC AUC per each experiment on CIFAR10 and SVHN datasets are presented in Table 5.

REFERENCES

- [1] Davide Abati, Angelo Porrello, Simone Calderara, and Rita Cucchiara. Latent space autoregression for novelty detection. In *Proceedings of the IEEE Conference on Computer Vision and Pattern Recognition*, pages 481–490, 2019.
- [2] Aisha Abdallah, Mohd Aizaini Maarof, and Anazida Zainal. Fraud detection system: A survey. *Journal of Network and Computer Applications*, 68:90–113, 2016.
- [3] Mohiuddin Ahmed, Abdun Naser Mahmood, and Md Rafiqul Islam. A survey of anomaly detection techniques in financial domain. *Future Generation Computer Systems*, 55:278–288, 2016.
- [4] Samet Akcay, Amir Atapour-Abarghouei, and Toby P Breckon. Ganomaly: Semi-supervised anomaly detection via adversarial training. In *Asian conference on computer vision*, pages 622–637. Springer, 2018.
- [5] Dario Amodei, Chris Olah, Jacob Steinhardt, Paul Christiano, John Schulman, and Dan Mané. Concrete problems in ai safety. *arXiv preprint arXiv:1606.06565*, 2016.
- [6] Jinwon An and Sungzoon Cho. Variational autoencoder based anomaly detection using reconstruction probability. *Special Lecture on IE*, 2:1–18, 2015.
- [7] Babak Ehteshami Bejnordi, Mitko Veta, Paul Johannes Van Diest, Bram Van Ginneken, Nico Karssemeijer, Geert Litjens, Jeroen AWM Van Der Laak, Meyke Hermesen, Quirine F Manson, Maschenka Balkenhol, et al. Diagnostic assessment of deep learning algorithms for detection of lymph node metastases in women with breast cancer. *Jama*, 318(22):2199–2210, 2017.
- [8] Raghavendra Chalapathy and Sanjay Chawla. Deep learning for anomaly detection: A survey. *arXiv preprint arXiv:1901.03407*, 2019.
- [9] Caroline Chan, Shiry Ginosar, Tinghui Zhou, and Alexei A Efros. Everybody dance now. In *Proceedings of the IEEE International Conference on Computer Vision*, pages 5933–5942, 2019.
- [10] Varun Chandola, Arindam Banerjee, and Vipin Kumar. Anomaly detection: A survey. *ACM computing surveys (CSUR)*, 41(3):1–58, 2009.
- [11] Xiaoran Chen and Ender Konukoglu. Unsupervised detection of lesions in brain mri using constrained adversarial auto-encoders. *arXiv preprint arXiv:1806.04972*, 2018.
- [12] Yunqiang Chen, Xiang Sean Zhou, and Thomas S Huang. One-class svm for learning in image retrieval. In *ICIP (1)*, pages 34–37. Citeseer, 2001.
- [13] Yong Shean Chong and Yong Haur Tay. Abnormal event detection in videos using spatiotemporal autoencoder. In *International Symposium on Neural Networks*, pages 189–196. Springer, 2017.
- [14] A. Chowdhury, D. V. Dyllov, Q. Li, M. MacDonald, D. E. Meyer, M. Marino, and A. Santamaria-Pang. Blood vessel characterization using virtual 3d models and convolutional neural networks in fluorescence microscopy. *IEEE ISBI 2017*, pages 629–632, April 2017.
- [15] Leon A Gatys, Alexander S Ecker, and Matthias Bethge. Image style transfer using convolutional neural networks. In *Proceedings of the IEEE Conference on Computer Vision and Pattern Recognition*, pages 2414–2423, 2016.
- [16] Izhak Golan and Ran El-Yaniv. Deep anomaly detection using geometric transformations. In *Advances in Neural Information Processing Systems*, pages 9758–9769, 2018.
- [17] Dong Gong, Lingqiao Liu, Wufeng Le, Budhaditya Saha, Moussa Reda Mansour, Svetha Venkatesh, and Anton van den Hengel. Memorizing normality to detect anomaly: Memory-augmented deep autoencoder for unsupervised anomaly detection. In *Proceedings of the IEEE International Conference on Computer Vision*, pages 1705–1714, 2019.
- [18] Ian Goodfellow, Jean Pouget-Abadie, Mehdi Mirza, Bing Xu, David Warde-Farley, Sherjil Ozair, Aaron Courville, and Yoshua Bengio. Generative adversarial nets. In *Advances in neural information processing systems*, pages 2672–2680, 2014.
- [19] Ari Heljakka, Arno Solin, and Juho Kannala. Pioneer networks: Progressively growing generative autoencoder. In *Asian Conference on Computer Vision*, pages 22–38. Springer, 2018.
- [20] Geoffrey E Hinton and Ruslan R Salakhutdinov. Reducing the dimensionality of data with neural networks. *science*, 313(5786):504–507, 2006.
- [21] Xun Huang, Ming-Yu Liu, Serge Belongie, and Jan Kautz. Multi-modal unsupervised image-to-image translation. In *Proceedings of the European Conference on Computer Vision (ECCV)*, pages 172–189, 2018.
- [22] Justin Johnson, Alexandre Alahi, and Li Fei-Fei. Perceptual losses for real-time style transfer and super-resolution. In *European conference on computer vision*, pages 694–711. Springer, 2016.

TABLE 5: ROC AUC in % with std on CIFAR 10 and SVHN per each class. For methods results are reported in two options: ROC AUC obtained with authors’ default hyperparameters (default), ROC AUC obtained with hyperparameters found by cross-validation (weakly s.)

CIFAR10											
	hyperparams	plane	car	bird	cat	deer	dog	frog	horse	ship	truck
Deep GEO	default	75.4±0.9	96.0±0.2	79.9±1.9	73.6±0.2	87.4±0.4	87.6±0.7	85.2±0.9	95.1±0.1	94.3±0.0	91.3±0.3
	weakly-s.	75.7±1.0	96.0±0.2	80.4±1.1	72.9±0.9	88.0±0.2	86.3±0.9	84.6±0.5	95.4±0.0	94.3±0.2	91.4±0.5
PIAD	default	81.8±0.1	87.1±0.3	74.9±0.3	60.7±0.2	78.1±0.5	70.6±1.4	81.7±0.8	84.4±0.4	86.3±0.4	82.3±0.6
	weakly-s.	84.3±0.2	86.7±1.1	74.4±0.9	59.6±2.1	85.0±1.1	73.6±1.1	83.8±1.2	87.0±1.1	88.8±0.2	89.4±0.7
Deep IF	default	85.2±1.2	94.3±0.4	72.5±4.0	76.8±1.2	89.9±0.7	86.1±1.0	90.3±1.7	89.1±1.0	92.0±1.0	95.6±0.1
	weakly-s.	87.1±0.9	97.0±0.3	75.2±2.9	73.7±1.8	88.9±1.0	85.0±2.6	90.5±0.9	86.3±1.7	93.4±0.3	95.7±0.3
Ours	weakly-s.	86.5±0.2	92.2±0.3	76.8±0.6	58.7±1.2	85.1±0.4	77.7±0.9	88.9±0.1	89.1±0.2	91.4±0.5	92.2±0.4
SVHN											
		0	1	2	3	4	5	6	7	8	9
Deep GEO	default	89.0±0.6	84.1±1.1	96.9±0.1	91.3±0.3	97.3±0.0	96.2±0.3	96.0±0.2	98.2±0.1	86.4±0.3	97.4±0.1
	weakly-s.	90.6±0.6	84.8±0.6	97.2±0.2	91.1±0.1	97.5±0.1	96.3±0.0	96.2±0.2	98.4±0.0	85.6±0.9	97.6±0.2
PIAD	default	85.6±0.4	79.2±1.1	74.8±0.4	69.2±0.0	77.3±0.8	74.6±0.9	76.3±0.7	77.5±0.4	78.0±0.2	77.4±0.3
	weakly-s.	86.3±0.9	80.2±0.9	76.2±0.8	71.4±1.1	77.0±0.5	71.9±0.9	70.6±0.5	78.4±0.2	79.6±0.7	71.9±0.8
Deep IF	default	65.3±1.1	68.7±1.8	51.9±0.8	57.1±1.5	56.7±2.1	64.9±1.5	50.9±0.8	56.2±1.9	63.7±0.9	54.3±1.1
	weakly-s.	75.0±1.2	70.5±1.5	51.1±0.8	59.0±0.9	57.7±1.4	68.4±0.6	54.5±0.2	58.7±0.7	69.6±1.6	59.1±1.5
Ours	weakly-s.	88.4±0.2	82.7±0.8	80.0±0.8	72.9±0.1	79.1±0.7	77.4±0.7	78.0±0.8	79.0±0.2	83.5±0.2	82.1±0.3

- [23] Tero Karras, Timo Aila, Samuli Laine, and Jaakko Lehtinen. Progressive growing of gans for improved quality, stability, and variation. *arXiv preprint arXiv:1710.10196*, 2017.
- [24] B Kiran, Dilip Thomas, and Ranjith Parakkal. An overview of deep learning based methods for unsupervised and semi-supervised anomaly detection in videos. *Journal of Imaging*, 4(2):36, 2018.
- [25] S. Kothari, J. H. Phan, T. H. Stokes, and M. D. Wang. Pathology imaging informatics for quantitative analysis of whole-slide images. *Journal of the American Medical Informatics Association: JAMIA*, 20(6):1099–1108, 2013.
- [26] Alex Krizhevsky and Geoffrey Hinton. Learning multiple layers of features from tiny images. Technical report, Citeseer, 2009.
- [27] Donghwoon Kwon, Hyunjo Kim, Jinoh Kim, Sang C Suh, Ikkyun Kim, and Kuinam J Kim. A survey of deep learning-based network anomaly detection. *Cluster Computing*, pages 1–13, 2017.
- [28] Fei Tony Liu, Kai Ming Ting, and Zhi-Hua Zhou. Isolation forest. In *2008 Eighth IEEE International Conference on Data Mining*, pages 413–422. IEEE, 2008.
- [29] Geoffrey J McLachlan and David Peel. *Finite mixture models*. John Wiley & Sons, 2004.
- [30] Mehdi Mohammadi, Ala Al-Fuqaha, Sameh Sorour, and Mohsen Guizani. Deep learning for iot big data and streaming analytics: A survey. *IEEE Communications Surveys & Tutorials*, 20(4):2923–2960, 2018.
- [31] Yuval Netzer, Tao Wang, Adam Coates, Alessandro Bissacco, Bo Wu, and Andrew Y Ng. Reading digits in natural images with unsupervised feature learning. 2011.
- [32] Anh Nguyen, Jason Yosinski, and Jeff Clune. Deep neural networks are easily fooled: High confidence predictions for unrecognizable images. In *Proceedings of the IEEE conference on computer vision and pattern recognition*, pages 427–436, 2015.
- [33] Khalil Ouardini, Huijuan Yang, Balagopal Unnikrishnan, Manon Romain, Camille Garcin, Houssam Zenati, J Peter Campbell, Michael F Chiang, Jayashree Kalpathy-Cramer, Vijay Chandrasekhar, et al. Towards practical unsupervised anomaly detection on retinal images. In *Domain Adaptation and Representation Transfer and Medical Image Learning with Less Labels and Imperfect Data*, pages 225–234. Springer, 2019.
- [34] Emanuel Parzen. On estimation of a probability density function and mode. *The annals of mathematical statistics*, 33(3):1065–1076, 1962.
- [35] Pramuditha Perera, Ramesh Nallapati, and Bing Xiang. Ocgan: One-class novelty detection using gans with constrained latent representations. In *Proceedings of the IEEE Conference on Computer Vision and Pattern Recognition*, pages 2898–2906, 2019.
- [36] Lukas Ruff, Nico Gornitz, Lucas Deecke, Shoaib Ahmed Siddiqui, Robert Vandermeulen, Alexander Binder, Emmanuel Müller, and Marius Kloft. Deep one-class classification. In *International Conference on Machine Learning*, pages 4390–4399, 2018.
- [37] Mohammad Sabokrou, Mohammad Khalooei, Mahmood Fathy, and Ehsan Adeli. Adversarially learned one-class classifier for novelty detection. In *Proceedings of the IEEE Conference on Computer Vision and Pattern Recognition*, pages 3379–3388, 2018.
- [38] Thomas Schlegl, Philipp Seeböck, Sebastian M Waldstein, Ursula Schmidt-Erfurth, and Georg Langs. Unsupervised anomaly detection with generative adversarial networks to guide marker discovery. In *International Conference on Information Processing in Medical Imaging*, pages 146–157. Springer, 2017.
- [39] Yu-Xing Tang, You-Bao Tang, Mei Han, Jing Xiao, and Ronald M Summers. Deep adversarial one-class learning for normal and abnormal chest radiograph classification. In *Medical Imaging 2019: Computer-Aided Diagnosis*, volume 10950, page 1095018. International Society for Optics and Photonics, 2019.
- [40] David MJ Tax and Robert PW Duin. Support vector data description. *Machine learning*, 54(1):45–66, 2004.
- [41] Nina Tuluptceva, Bart Bakker, Irina Fedulova, and Anton Konushin. Perceptual image anomaly detection. In Shivakumara Palaiahnakote, Gabriella Sanniti di Baja, Liang Wang, and Wei Qi Yan, editors, *Pattern Recognition*, pages 164–178, Cham, 2020. Springer International Publishing.
- [42] Abhishek Vahadane, Tingying Peng, Amit Sethi, Shadi Albarqouni, Lichao Wang, Maximilian Baust, Katja Steiger, Anna Melissa Schlitter, Irene Esposito, and Nassir Navab. Structure-preserving color normalization and sparse stain separation for histological images. *IEEE transactions on medical imaging*, 35(8):1962–1971, 2016.
- [43] Xiaosong Wang, Yifan Peng, Le Lu, Zhiyong Lu, Mohammad-hadi Bagheri, and Ronald M Summers. Chestx-ray8: Hospital-scale chest x-ray database and benchmarks on weakly-supervised classification and localization of common thorax diseases. In *Proceedings of the IEEE conference on computer vision and pattern recognition*, pages 2097–2106, 2017.
- [44] Graham Williams, Rohan Baxter, Hongxing He, Simon Hawkins, and Lifang Gu. A comparative study of rnn for outlier detection in data mining. In *2002 IEEE International Conference on Data Mining*, 2002. *Proceedings.*, pages 709–712. IEEE, 2002.
- [45] Houssam Zenati, Manon Romain, Chuan-Sheng Foo, Bruno Lecouat, and Vijay Chandrasekhar. Adversarially learned anomaly detection. In *2018 IEEE International Conference on Data Mining (ICDM)*, pages 727–736. IEEE, 2018.
- [46] Shuangfei Zhai, Yu Cheng, Weining Lu, and Zhongfei Zhang. Deep structured energy based models for anomaly detection. *arXiv preprint arXiv:1605.07717*, 2016.
- [47] Richard Zhang, Phillip Isola, Alexei A Efros, Eli Shechtman, and

- Oliver Wang. The unreasonable effectiveness of deep features as a perceptual metric. In *Proceedings of the IEEE Conference on Computer Vision and Pattern Recognition*, pages 586–595, 2018.
- [48] Chong Zhou and Randy C Paffenroth. Anomaly detection with robust deep autoencoders. In *Proceedings of the 23rd ACM SIGKDD International Conference on Knowledge Discovery and Data Mining*, pages 665–674, 2017.
- [49] Bo Zong, Qi Song, Martin Renqiang Min, Wei Cheng, Cristian Lumezanu, Daeki Cho, and Haifeng Chen. Deep autoencoding gaussian mixture model for unsupervised anomaly detection. In *International Conference on Learning Representations*, 2018.